Design and Applications of a Dual-Wavelength Digital Holography Wavefront Sensor

James Mitchell[1*] and Stanislav Gordeyev[1]

[1]Aerospace and Mechanical Engineering Department, University of Notre Dame, Notre Dame, Indiana 46556

ABSTRACT

The design and validation of a dual-wavelength digital holography wavefront sensor for quantitative simultaneous measurements of aero-optical wavefronts in subsonic compressible flow over two apertures is presented. The optical setup and processing methodology for reconstructing independently-reconstructed optical path difference (OPD) fields from interference patterns generated by two laser beams separated spatially along the streamwise axis are described in detail. The agreement and accuracy of the reconstructed wavefronts in a turbulent boundary layer flow are assessed, and the error between the OPD fields reconstructed from each beam is quantified using a normalized L_2-norm relative error metric. In addition, a time-delayed cross-correlation between the separated beams was computed to estimate the convective speed of aero-optical distortions in the boundary-layer-dominated flow. We demonstrate the consistent agreement between the two OPD fields, with errors being largely independent of flow speed, and convective speeds that scale predictably with freestream flow speed. These results validate dual-wavelength digital holography as a reliable method of high-resolution wavefront sensing in compressible flow environments.

1. INTRODUCTION

When light travels through a flow field with varying spatial density, the light beam becomes distorted, as the index of refraction, n, is proportional to the density,

$$n(x, y, z, t) = 1 + K_{GD}\rho(x, y, z, t), \tag{1}$$

where K_{GD} is the Gladstone-Dale constant. The resulting aero-optical distortions, denoted as the Optical Path Difference (OPD), are proportional to the integral of the fluctuating density field,

$$OPD(x, y, t) = K_{GD} \int \rho'(x, y, z, t) dz \ , \tag{2}$$

where the integration is performed in the beam propagation direction.[1,2] These optical distortions can significantly affect the propagation of the beam, leading to loss of intensity of the beam and deterioration (blurring) of visual representations of objects.[1,3] Therefore, careful measurements and analysis of the wavefronts, distorted by turbulent flows, are essential to study the sources of aero-optical distortions and various means to mitigate them. Two most common wavefront sensors to measure spatiotemporally resolved wavefronts are the Shack–Hartmann wavefront sensor (SHWFS) and the digital holographic wavefront sensor (DHWFS). While SHWFS has been extensively used for many decades now,[1] DHWFS as a sensor to measure aero-optical distortions was introduced only recently,[4,5] and it is rapidly gaining popularity due to better spatial resolution compared to SHWFS, as well as better performance in the presence of shock-related wavefront gradients.[6]

The principle of operation of the Digital Holography sensor is presented in Fig. 1. The continuous laser beam with a large coherence length is split into two beams: a signal and a reference beam. The signal beam goes through a flow of interest and collects wavefront distortions along its path. It is then combined with the reference beam from the same laser source at a focal plane of a digital camera to form an interference pattern. The tilt mirror is used to add a small angle between the signal and the reference beams before combining them on the sensor.

*Corresponding author: jmitch24@nd.edu

Unconventional Imaging, Sensing, and Adaptive Optics 2025, edited by Jean Dolne, Santasri Bose-Pillai, Matthew Kalensky, Proc. of SPIE Vol. 13619, 136190K · 2025 Published by SPIE
0277-786X · doi: 10.1117/12.3063911

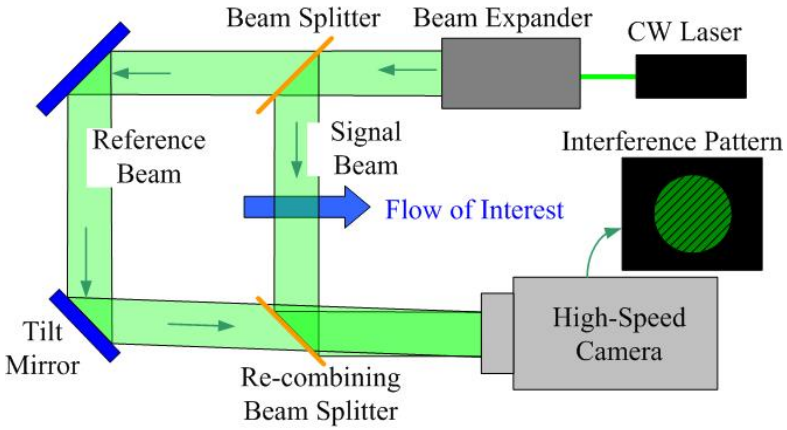

Figure 1: Schematic of the digital holography sensor.

The total intensity of the fringe pattern, I, is the superposition of the complex optical fields of the signal and reference beams, U_S and U_R, respectively.

$$I = |U_S + U_R|^2 = |U_S|^2 + |U_R|^2 + U_S U_R^* + U_S^* U_R, \tag{3}$$

where the asterisk denotes complex conjugate. The terms $|U_S|^2$ and $|U_R|^2$ are the real-only terms which are ignored as they do not contribute to the phase information imposed on the signal beam.[7] An example of the interferometry pattern is shown in Fig. 2(a). Both $U_S U_R^*$ and $U_S^* U_R$ contain the wavefront distortion information, but since $U_S U_R^*$ and $U_S^* U_R$ are complex conjugates of each other, only one term is needed to find the distorted optical complex field. To isolate the $U_S U_R^*$-term from the other terms, a two-dimensional spatial Fourier transform of the hologram image is performed. The result is presented in Fig. 2(b). The position of $U_S U_R^*$ in the Fourier space depends on the relative angle between the signal and the reference beams on the image plane, and it can be shifted in the Fourier space by moving the tilt mirror and separating this term from the contaminating effects of the central (real-only) term in the Fourier space. All unwanted terms (i.e. $U_S^* U_R$, $|U_S|^2$ and $|U_R|^2$) are filtered out by selecting only the off-axis peak circled in orange in Fig. 2(b). After isolating $U_S U_R^*$, the inverse Fourier transform is performed to recover both the amplitude and the phase of the distorted wavefront field. The resulting phase field is shown in Fig. 2(c).

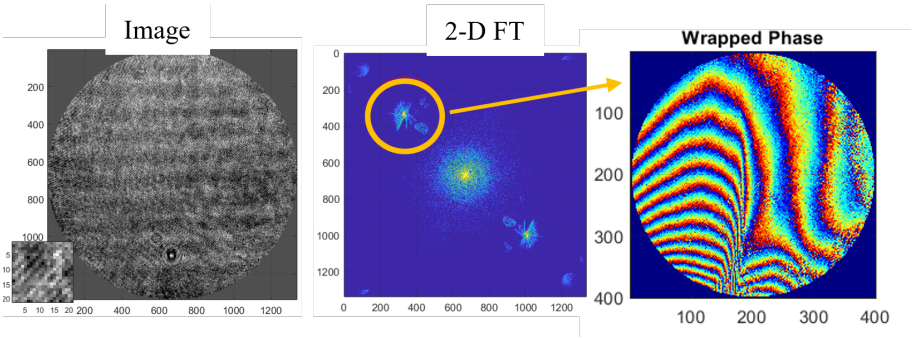

(a) (b) (c)

Figure 2: (a) The holographic image and (b) its Fourier transform. After selecting the signal-related peak, indicated by an orange circle, the Inverse Fourier Transform is performed to recover the wavefront phase, shown in (c).

By definition, the phase is wrapped between $-\pi$ and π and must be unwrapped before it can be related to a wavefront. There are several algorithms for unwrapping the phase,[8,9] but in general they cannot correctly unwrap the phase map when sharp wavefront gradients are present. For sufficiently large phase changes, it will result in

the phase differences between two adjacent pixels being larger than 2π, leading to a non-unique reconstruction of the phase field. To address this problem, a dual-wavelength DH sensor is proposed.[10–14] For dual-wavelength DH sensors, two co-aligned beams with different wavelengths, λ_1 and λ_2, are propagated through the flow of interest, and two wrapped phase maps at these wavelengths are simultaneously measured. The difference between two wrapped phase maps results in a new "effective" phase map, which corresponds to a longer "effective" wavelength, $\lambda_{eff} = \frac{\lambda_1 \lambda_2}{|\lambda_1 - \lambda_2|}$. By properly selecting two distinct wavelengths, physical phase changes of the measured optical field at the "effective" wavelength can be made to be between $-\pi$ and π, enabling correct phase unwrapping. Thus, dual-wavelength DH sensors reduce or even eliminate ambiguity during the unwrapping process.

Because both phase maps are simultaneously measured using the same digital sensor, the dual-wavelength DH sensor can also be used to measure wavefronts over two different regions. To do that, signal laser beams are optically separated and sent through different regions of the flow. After that, they are combined on the digital sensor with their corresponding reference beams. By imposing different tilts on the reference beams, the corresponding $U_S U_R^*$-terms can be separated in the Fourier space, and isolated and analyzed individually by implementing the filtering technique, as discussed before.

2. EXPERIMENTAL SETUP

All measurements were performed in the Trisonic Wind Tunnel (TWT) at Hessert Laboratory for Aerospace Research at the University of Notre Dame. The TWT is a continuous flow indraft wind tunnel with an inlet contraction ratio of 150:1. The test section is constructed of aluminum, with a cross section of 10 cm x 9.9 cm and a length of 160 cm from the end of the inlet to the diffuser. Optical access windows are installed on the walls of the test section from 130 cm to 150 cm. The freestream velocity was measured using a Pitot probe just upstream of the optical window. The aero-optical flow of interest was a boundary layer formed over the tunnel walls, and the development length of the boundary layer from the end of the inlet to the measurement location is $L = 148$. Using the equation of the growth of the boundary thickness on the flat plate, the thickness of the boundary layer, δ, at the measurement location was estimated to be approximately between 22 mm at $M = 0.5$ and 18 mm at $M = 0.75$. A schematic of the TWT facility can be seen in Figure 3.

The schematic and labeled picture of the dual-wavelength DH sensor are shown in Fig 4 and Fig 5, respectively. The lasers chosen for this optical setup were the Cobolt 05-01 Series with 532 nm light and the Cobolt 05-01 Series with 640 nm light. Both lasers have a coherence length greater than 100 m, which is sufficient for current experiments. For this experiment, in which maximizing the effective wavelength was not required, the wavelengths were selected based on their ability to be cleanly separated by dichroic filters. At the beginning of the optical path, both beams, each 0.7 mm in diameter, are guided using two steering mirrors into spatial filters comprised of a microscopic objective and a 10 micron pinhole, resulting in an Airy pattern in the far field. An iris along each path clips out the Airy rings, and f=250 mm lenses collimate each beam to 1 inch in diameter. Each expanded beam then passes through its own 1.5" beam cube with a 50/50 transmission/reflection ratio, separating the signal and reference beams of each wavelength. The two signal beams are then sent through a 2" dichroic filter (DMLP567L, Thorlabs, USA) which *transmits* the 640 nm beam and *reflects* the 532 nm beam. This filter is placed along a rail to allow the beams to fully overlap or be separated by a variable distance at the tunnel window. The setup in Fig. 5 shows the case of both beams fully overlapping in order to perform simultaneous measurements of the same flow region. A large return mirror is placed on the far side of the tunnel, and the signal beams are returned along the same paths until they pass through the same 50/50 beam cubes mentioned previously. The reflected light as they pass through the beam cubes is unused, while the transmitted light is recombined using a *different* dichroic filter (DMSP567L, Thorlabs, USA) which, unlike the first dichroic filter, *reflects* the 640 nm beam and *transmits* the 532 nm beam. The combined signal beams are re-imaged using two consecutive 4f relay systems: the first composed of lenses with focal lengths of 400 mm and 350 mm, and the second with focal lengths of 175 mm and 200 mm, respectively. These focal lengths are specific to the distance to the tunnel in our setup, and they re-image the image plane of the return mirror to the camera plane while having the property of 1x magnification, outputting a 1" beam. In one of the focal planes of the re-imaging lenses, an iris is placed to clip out any unwanted ghost beams. After the re-imaging telescopes, the combined signal beams are reflected by a 2" 50/50 beam cube onto the digital sensor. This beam cube is placed very close

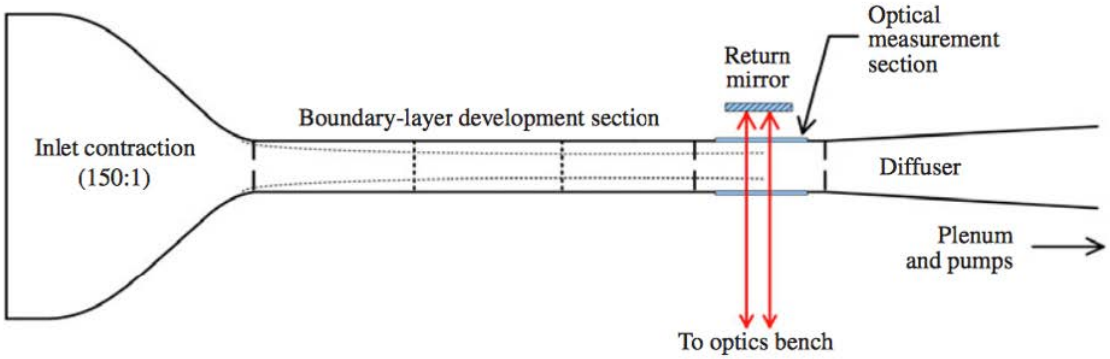

Figure 3: Schematic of TWT facility outlining the location of the measurement section, orientation of the beams and the location of the return mirror.

to the digital sensor in order to impart a variable tip and tilt on each of the signal beams without imparting a large translational displacement that would move the signal beams off of the digital sensor.

Each of the reference beams, as they are separated from their respective signal beams by the cube beam splitters, is reflected by a series of mirrors and recombined using a 50/50 beam splitter. The 532 nm beam path has two mirrors prior to transmission through the beam splitter, while the 640 nm beam path has a single mirror, and uses the beam splitter as the other beam control component. These components are used to add tip and tilt to the reference beams, while ensuring overlap with the signal beams on the camera. The 50/50 beam cube also serves the role of a beam intensity filter, so that the signal and reference beams are close to equal in intensity on the digital sensor. This results in the strongest interference pattern and the highest signal-to-noise ratio. In order to maximize the strength of the interference pattern, neutral density (ND) filters may be placed along any appropriate part of the optical path. In our setup, small intensity reductions of the red signal beam by the dichroic filters required the placement of a weak ND filter along a part of the optical path where the green signal beam was isolated (not labeled in Fig 5).

The partially overlapping reference beams are then expanded by a factor of 1.5 using f = -200 mm and f = 300 mm lenses (not labeled in Fig 5 to avoid clutter) to facilitate the introduction of significant tip and tilt in the reference beams while maintaining full overlap between the signal and reference beams on the digital sensor. The reference beam then passes through the final 2" beam cube, combining the signal and reference beams and fully overlapping them on the high-speed camera.

The resulting interference pattern was captured using a Phantom v2512 high-speed camera with a pixel width of 28 microns and a resolution of 768 x 768 pixels.

Static and total pressure measurements were taken by a Pitot probe, installed in the middle of the measurement section, and used to find the freestream Mach number, using the isentropic relation,

$$\frac{p}{p_t} = \left(1 + \frac{\gamma - 1}{2} M^2\right)^{-\frac{\gamma}{\gamma - 1}}. \tag{4}$$

The freestream velocity, $U_\infty = M \cdot a$, was calculated using the adiabatic relation for the local speed of sound, a,

$$a = \sqrt{\frac{\gamma R T_0}{1 + \frac{\gamma - 1}{2} M^2}}, \tag{5}$$

where $\gamma = 1.4$ is the specific heat ratio of air, $R = 287\ J/(kg \cdot K)$ is the universal gas constant for air, and $T_0 = 297$ K is the stagnation temperature of the flow.

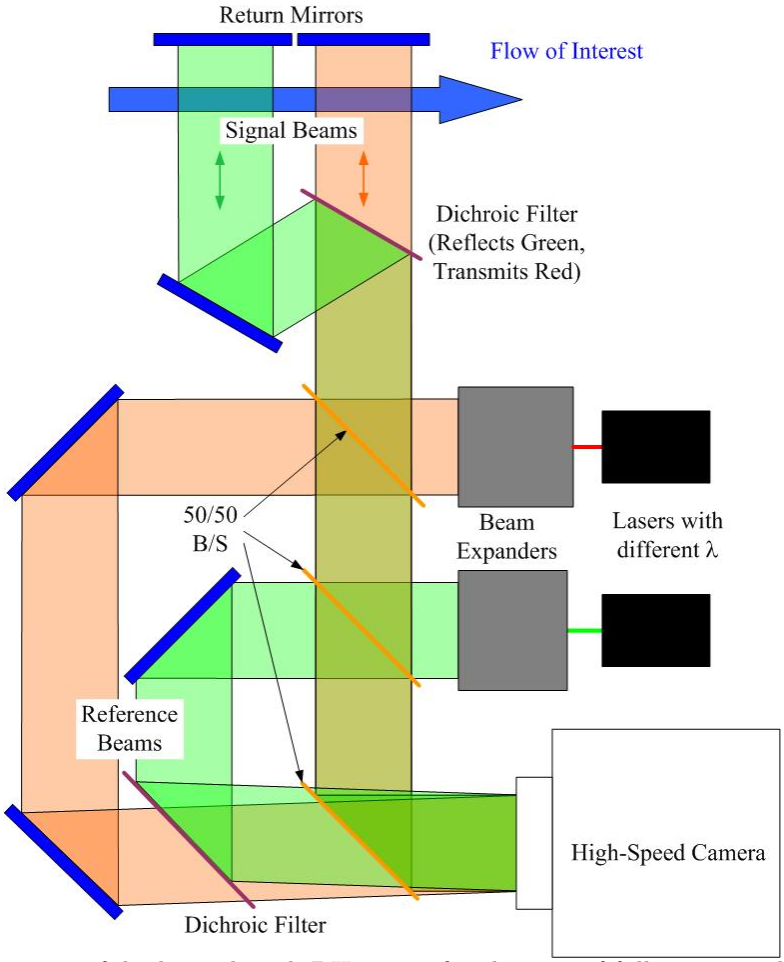

Figure 4: Schematic of dual-wavelength DH sensor for the case of fully separated signal beams.

The aero-optical measurements were acquired at three different separations between the green and red beam paths: 0mm (later called a fully overlapping case), 40mm (or 2δ), and 60mm (or 3δ), each at five different Mach numbers of 0.52, 0.59, 0.65, 0.70, and 0.73. For the non-overlapping cases, the green beam was placed upstream of the red beam. A total of 4,300 frames of data were taken for each case at a frequency of 39 kHz. The laser power levels were set to 600 mW, and the frame exposure time was 3 μs.

3. DATA REDUCTION AND ANALYSIS

The process of reconstructing the corresponding wavefronts from the digital holographic image for each wavelength is as follows. The first step is to subtract out the mean pixel value of the image in order to remove the DC offset in the Fourier plane. Then, the image is cropped tightly, so that the overlapping region is centered within a square aperture to reduce the number of pixels to be analyzed and improve the signal-to-noise ratio in the Fourier plane. A representative example is shown in Fig. 6(a). Then, the Matlab function fft2 is used to take a spatial 2-dimensional Fast Fourier Transform of the cropped image. In the Fourier plane, shown in Fig. 6(b), there is a strong, central zero-order peak and two weaker cross-correlation peaks for each wavelength. Since for a given beam, the two off-center peaks are complex conjugates of one another, as indicated in Equation 3, they carry the same information, and only one is needed for reconstructing the wavefront. Each cross-correlation peak, related to either the green or the red laser beam, and circled in Fig. 6(b), is then centered within a round aperture for each of the beams. The spatial resolution of the reconstructed wavefront is equal to the pixel-wise dimensions of this circular crop, but an increased radius also will include more noise from the zero-order peak,

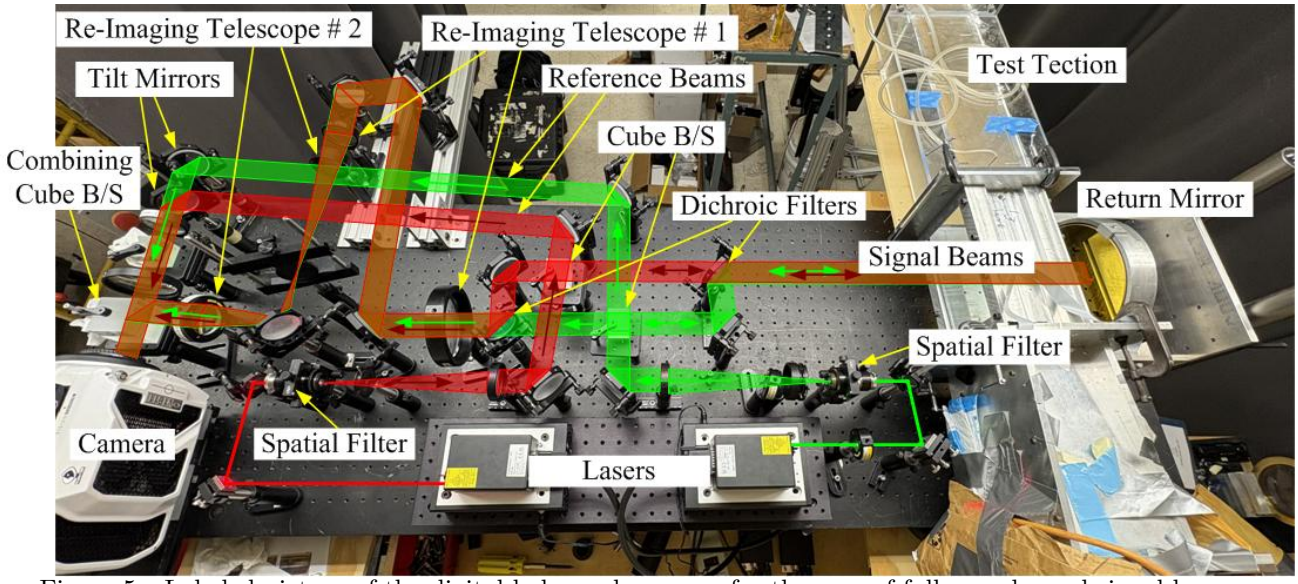

Figure 5: Labeled picture of the digital holography sensor for the case of fully overlapped signal beams.

leading to a smaller signal-to-noise ratio.

After the crop, an inverse 2-dimensional Fourier transform is performed on each circular aperture using the Matlab function ifft2, resulting in the 2π-wrapped wavefront. The unwrapped no-flow wavefront, shown in Fig. 6(c-d) for the red beam and the green beam, respectively, is then subtracted from the flow case and a circular mask is applied to the wrapped wavefront to mask any noise surrounding the circular overlap region, greatly improving unwrapping performance. All pixels outside the chosen circular aperture are converted to NaNs.

To recover OPD from the wrapped phase, we performed phase unwrapping using the least squares method, which minimizes the sum of squared differences between the gradient of the unwrapped phase solution and that of the measured wrapped phase.

At this point, tip/tilt and piston are calculated for the reconstructed wavefront using a least-squares plane fit and then subtracted from the wavefront. The resulting wavefronts are plotted in Fig. 6(e-f) the red beam and the green beam, respectively. As expected for the fully overlapping beam case, the wavefronts should be very similar, which is indeed the case in these subplots.

Ghost beams caused by back-reflections in beam cubes or other optical components may appear in the Fourier plane in Fig. 6(b). The circular Fourier aperture should also be used to crop out these ghosts as best as possible to avoid nonphysical contributions to the reconstructed OPD. Ghost beams that could not be eliminated using a crop in the Fourier plane created fringes in the OPD field. An example of this is shown in Fig. 7(a). In order to eliminate these additional ghost beams, a second spatial 2-dimensional Fast Fourier Transform was taken of the data (see Fig. 7(b)), and local masks were applied in Fourier space to the peaks corresponding with those fringes to suppress those frequencies. These masks are shown in Fig. 7(b) as white circles. All pixel values within the masks were set to 0, and an inverse FFT was performed to return the data to the spatial domain, with the final result plotted in Fig. 7(c). For each wavefront time series for each laser beam, the time-averaged wavefront was subtracted from each frame to eliminate the effects of steady lensing. Finally, all resulting OPD data were divided by $2\sqrt{2}$ to account for the double-pass setup and the presence of two boundary layers on both tunnel walls.[15]

A small number of frames were excluded from analysis due to corruption, identified by an abnormally high fraction of zero-valued pixels. These frames were automatically flagged and replaced with NaN values prior to post-processing.

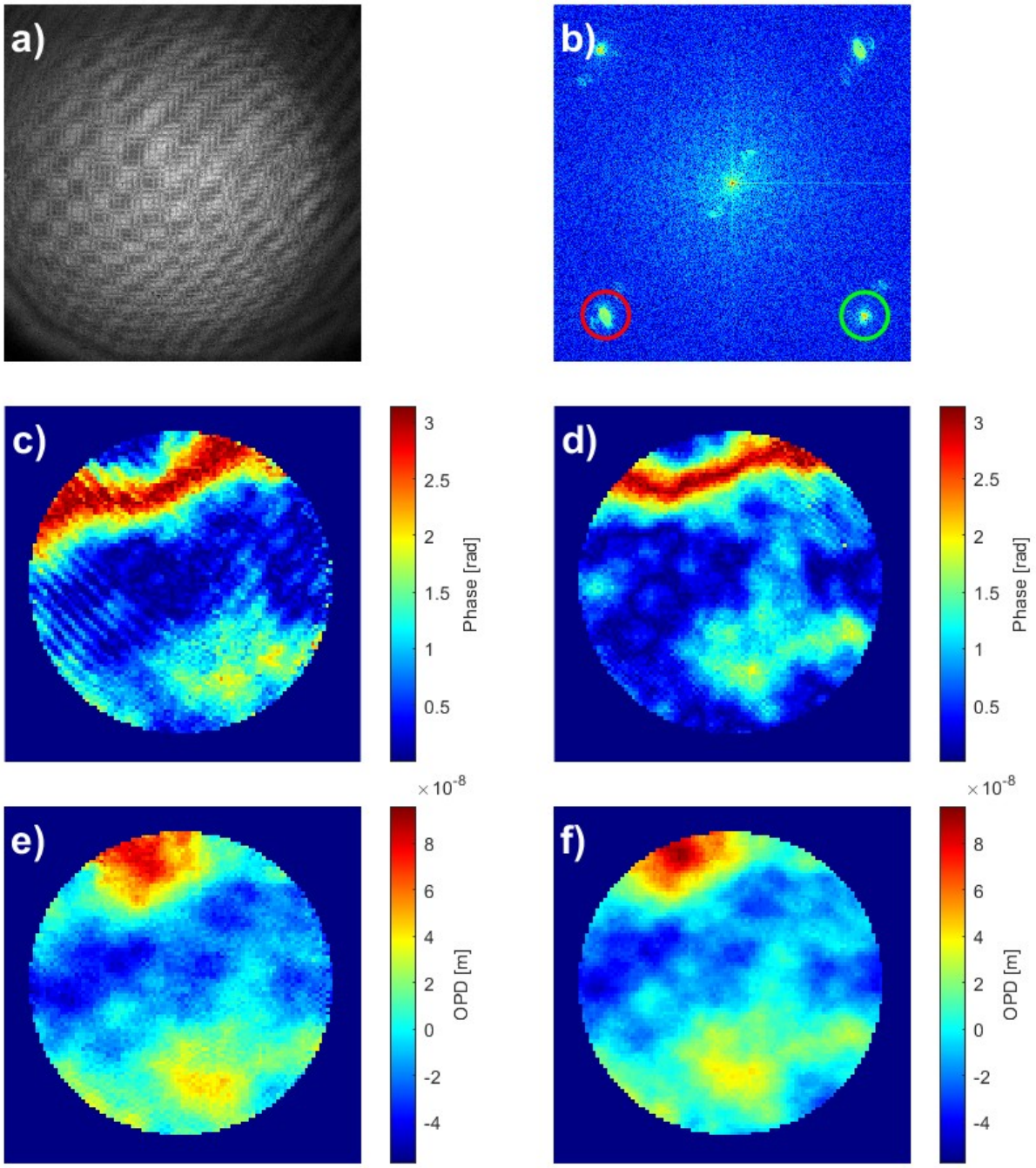

Figure 6: Typical wavefront reconstruction for dual-wavelength digital holography. (a) Raw holographic image after DC offset removal and cropping. (b) Fourier plane showing the cross-correlation peaks for each laser beam wavelength. (c) Red beam wrapped phase field obtained after inverse Fourier transform and masking. (d) Green beam wrapped phase field obtained after inverse Fourier transform and masking. (e) Red beam final wavefront after least-squares unwrapping, tip/tilt removal and time-averaged wavefront subtraction. (f) Green beam final wavefront after least-squares unwrapping, tip/tilt removal and time-averaged wavefront subtraction.

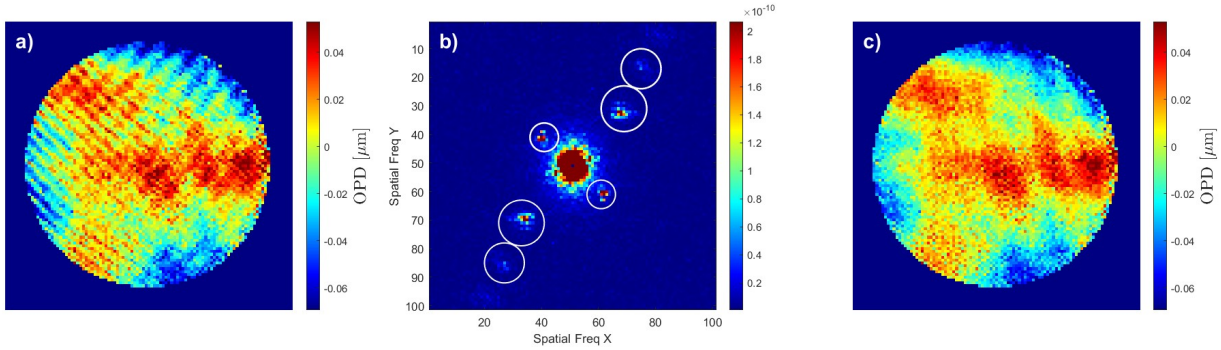

Figure 7: Fringe-removal due to the presence ghost beams using the Fourier masking. (a) OPD before the Fourier masking. (b) 2-D Fourier transform of the wavefront, with circles around the ghost beams regions to be masked (c) Reconstructed OPD after masking out the ghost beams and performing inverse 2-D Fourier transform.

4. RESULTS

4.1 Fully Overlapping Case

Even when the beams looked perfectly overlapped, a small offset was observed between the beams, mainly in the horizontal direction. This small shift can be seen in Figure 6(e-d). For each fully overlapping case, this offset was found and removed by minimizing the rms of the OPD field given by the difference between the green beam- and red beam-measured OPDs in order to perfectly align the beams. This difference between the wavefronts will be referred to in this paper as the differential OPD. After shifting one field to overlap with the other, only pixels shared between the original OPD fields were kept for analysis.

Figure 8 presents a side-by-side comparison of the OPD fields reconstructed from the red and green beams, together with the resulting differential OPD field. The same turbulent flow structures are clearly evident in both panels a) and b) of Figure 8, demonstrating that dual-wavelength DH can reliably measure the same optical field with two beams of different wavelengths.

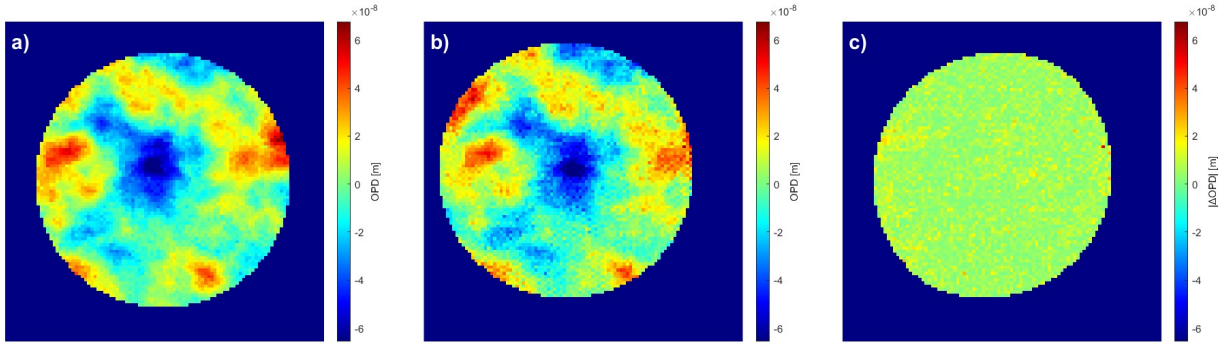

Figure 8: Reconstructed OPD fields for the fully overlapping case. (a) OPD measured with the green (532nm) wavelength. (b) OPD measured with the red (640nm) wavelength after shifting by the pixel offset. (c) Absolute value of the difference between the two fields after alignment.

The red beam OPD exhibits slightly higher noise levels than that of the green OPD, leading to granular noise patterns in the differential field. This increased noise in the red OPD field is likely a consequence of the fringe-removal filtering, which was applied only to the red wavefronts. Importantly, the absence of coherent structures in the differential OPD indicates that no significant systematic discrepancies exist between the two reconstructions, reinforcing the agreement between the red and green reconstructed OPD fields.

To quantify the relative error between wavefronts measured by two beams for the fully overlapped case, a relative error in L_2-norm, $\Sigma(t)$, was computed for each frame and for all Mach numbers, where $\Sigma(t)$ is given by

$$\Sigma(t) = \frac{\langle [OPD_1(x,y,t) - OPD_2(x,y,t)]^2 \rangle_{x,y}}{\langle [OPD_1(x,y,t)]^2 \rangle_{x,y}}, \tag{6}$$

and where the angular brackets indicate the spatial averaging over the aperture. In addition, the time-averaged value of the relative error, $\Sigma = \overline{\Sigma(t)}$, was also computed. The Σ values for the fully overlapped case are presented in Table 1.

Mach Number	Time-averaged Relative Error, $\overline{\Sigma(t)}$ (in %)
0.52	36.1
0.59	21.0
0.65	22.1
0.70	16.3
0.73	16.7

Table 1: Normalized errors for the fully overlapped beams at each flow speed.

The time-averaged normalized relative error shows a small downward trend with the increasing flow speed, suggesting that the observed disagreement arises primarily from sources which do not scale with flow speed.

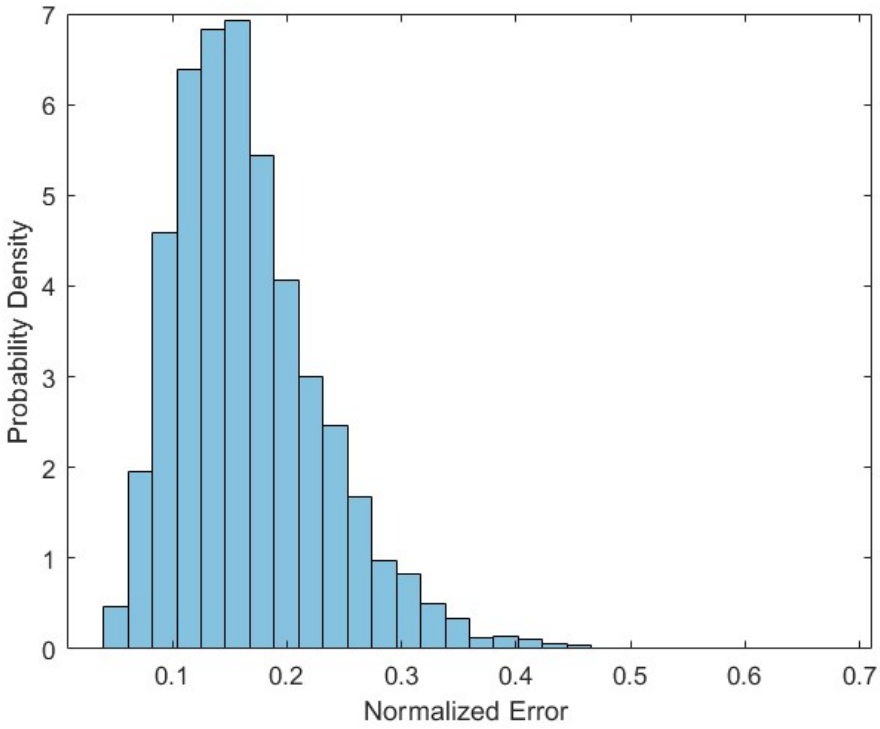

Figure 9: Probability density function of the normalized error, Eq. 6, between two fully overlapped beams for the Mach 0.73 case.

To further investigate the disagreement between the beams, we computed the probability density function (PDF) of the normalized relative error, $\Sigma(t)$, calculated using Eq. 6, for each frame. This distribution is presented in Figure 9 and characterizes the frame-to-frame variability of the spatial error, providing insight into the nature of, and potential causes of the error.

The peak of the distribution occurs at approximately 9% indicating that, typically, the disagreement between the red- and green-measured OPDs is relatively small, suggesting good agreement between the beams. However, the weak skewness of the distribution indicates that certain frames exhibit higher error values than would be expected from random noise alone, implying the existence of weak sources of systematic error between the OPD fields.

We also calculated the time-averaged spatial variation of each individual OPD field, for each flow speed, defined as

$$OPD_{rms} = \sqrt{\overline{\langle [OPD_1(x,y,t)]^2 \rangle_{x,y}}}. \tag{7}$$

The computed OPD_{rms} values for each beam are shown in Figure 10 for each flow speed case. If the two wavelength-reconstructed OPD_{rms} were in perfect agreement, one would expect OPD_{rms} values of the red and the green beams to be identical to each other for each of the flow speeds. In practice, the red beam consistently exhibits slightly higher OPD_{rms} values. This can be attributed to the higher levels of random noise in the wavefronts observed for the red beam (640 nm) data, as discussed previously. Despite this small difference between the OPD_{rms} values for both beams, the overall levels of aero-optical distortions agree quite well with the theoretical model, indicated as a dashed line in Figure 10, developed for the canonical boundary layers.[16]

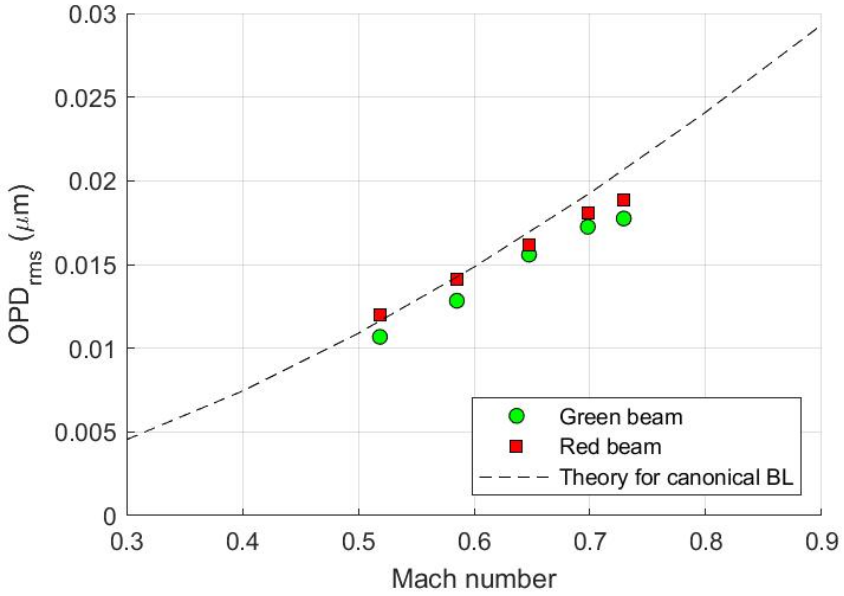

Figure 10: OPD_{rms} for each beam as a function of the freestream Mach number, and the comparison with the theoretical model for canonical boundary layers.[16]

4.2 Separated Beams Case

In the previous work,[17,18] SHWFS was used to collect and analyze wavefronts over two separate apertures using the same experimental facilities as in the present work. The purpose of that work was to investigate the convective nature of boundary-layer wavefronts to test the limits of the frozen field assumption, a model of simple convection. It was found that for large aperture separations of 3-4 boundary layer thicknesses, a convective-only model of wavefront propagation was not sufficient to characterize the downstream wavefront from upstream data.

One of the goals of the presented work is to continue studying possible ways to predict the wavefronts over the downstream aperture using the wavefronts collected over the upstream aperture. Thus, similar experiments were conducted using a dual-beam DHWFS for two separations between the red and the green beams of 40 mm (2δ) and 60 mm (3δ). The convective only model assumes that the aero-optical structures simply convect with a constant convective speed. To compute the relationship between freestream velocity and convective speed

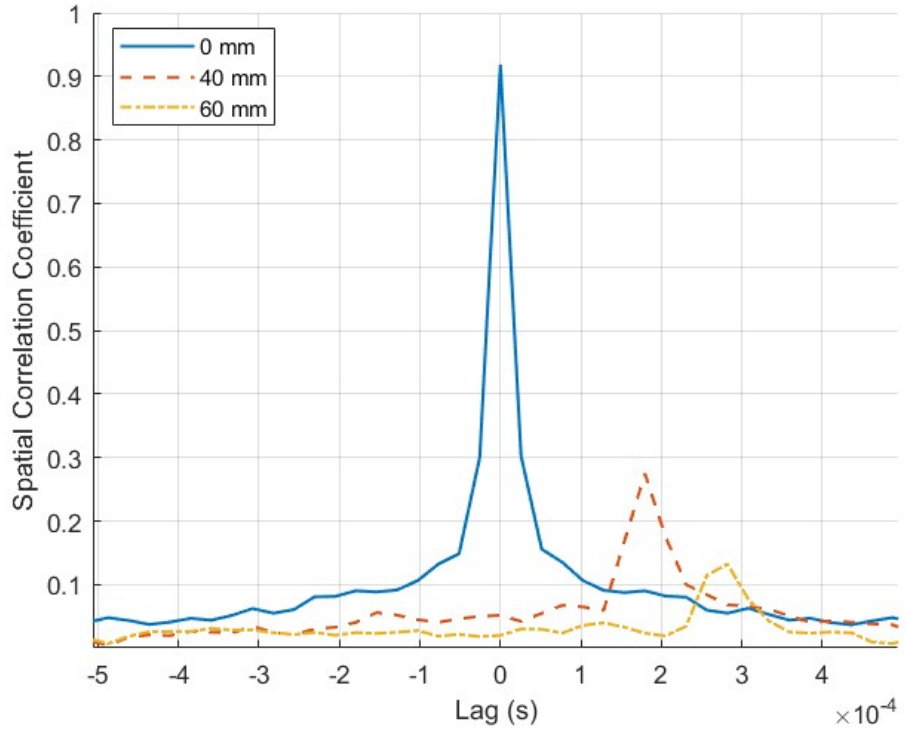

Figure 11: Cross-correlation as a function of time delay for the Mach 0.59 flow case.

of boundary layer aero-optical structures for a given flow speed, we performed a time-lagged cross-correlation between green- and red-beam OPD reconstructions for each of the three beam separations, including the fully overlapped case of 0 mm. For each pixel, the time series $OPD_1(x, y, t)$ and $OPD_2(x, y, t + \tau)$ are treated as vectors. For each pixel, the normalized correlation coefficient, or Pearson correlation coefficient, is given as

$$r_{xy}(\tau) = \frac{\sum_t \ OPD_1(x, y, t) OPD_2(x, y, t + \tau)}{\mu_{1,xy}\mu_{2,xy}} \tag{8}$$

where $\mu_{1,xy}$ and $\mu_{2,xy}$ are the temporal standard deviation of $OPD_1(x, y, t)$ and $OPD_1(x, y, t+\tau)$, respectively, for that pixel. The resulting correlation coefficients were then averaged across all pixels valid in both frames to obtain the frame-wise correlation coefficient for each time lag. Figure 11 shows one such cross-correlation function for all 3 spatial beam separations at Mach 0.59. The location of the peak represents the time delay required for the aero-optical structures to convect from the upstream aperture to the downstream aperture. The value of the peak is related to the degree to which the density fluctuations change spatially during the time they convect between the apertures. The normalized value of 1 means that the wavefronts are completely unchanged and simply convect between the apertures. The deviation of the value from 1 indicates the amount of warping of the density structures between the two apertures. For the separation of 40 mm $= 2\delta$, the peak value is about 0.3, and it drops further to 0.1 for the beam separation of 60 mm $= 3\delta$. This indicates that for these large beam separations, the aero-optical structures changed significantly between the apertures, which is consistent with similar observations.[17,18]

The time delay of the peak can be used to compute the convective speed of the wavefronts. To achieve a sub-frame temporal resolution, parabolic interpolation was applied to each cross-correlation peak to estimate the true time delays. Then, a line of best fit was applied to a plot of time lag versus spatial beam separation for each flow speed case, with the result shown in Figure 12 for the Mach 0.59 case. The convective flow speed is given by the slope of the best-fit line.

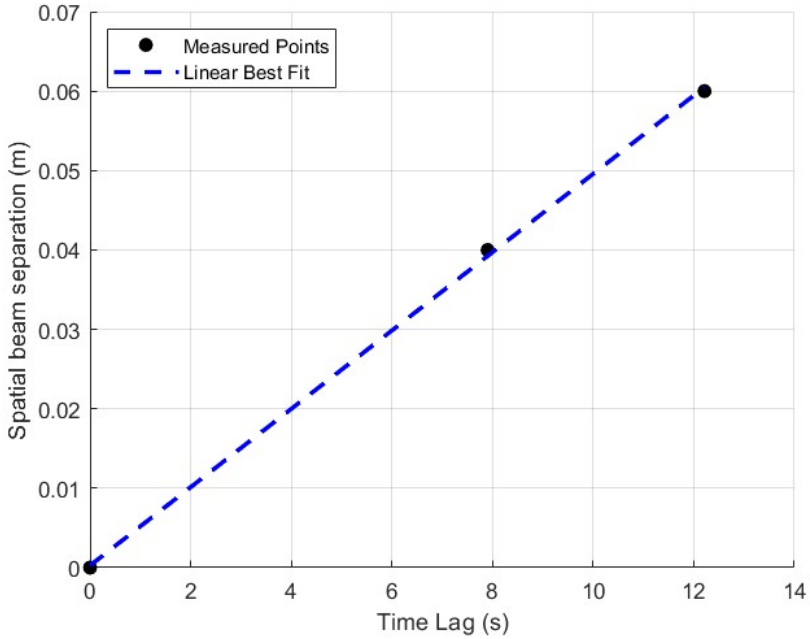

Figure 12: Example convective speed estimation for Mach 0.59 flow case. Spatial beam separations are plotted against the time lag corresponding to the peak of the time lag cross-correlation for each of the three separation distances. The slope of the linear best fit gives the convective speed of the aero-optical structures.

A table of cross-correlation-computed convective velocity, U_c, normalized by the corresponding freestream speeds, U_∞, measured by Pitot probe, is given in Table 2 for all measured Mach numbers. The convective speed measurements are consistently around 1.1x higher than the measured freestream values. These values are significantly larger than the expected convective speeds of the aero-optical distortions for the canonical subsonic boundary layers of $0.82U_\infty$.[16] The reason for this is unknown at this moment and is currently under investigation. Despite this, the cross-correlation analysis provides insight into the rate at which the flow-related wavefronts become uncorrelated for separate apertures.

M_{inf}	U_c/U_∞
0.52	1.10
0.59	1.12
0.65	1.15
0.70	1.13
0.73	1.16

Table 2: Freestream velocity and the ratio between convective and freestream velocities, for each flow speed.

5. CONCLUSIONS

In this paper, we presented the design, implementation, and validation of a dual-wavelength digital holography wavefront sensor for quantitative imaging of boundary layer aero-optical distortions. The sensor reconstructs optical path difference fields from two spatially separated laser beams of different wavelengths, enabling high-resolution measurement of density-induced wavefront distortions simultaneously at multiple spatial locations. To study the validation of the sensor, we measured aero-optical distortions over both the fully overlapped and the separated beams in a subsonic compressible boundary layer flow at the Trisonic Wind Tunnel facility at Hessert Laboratory for Aerospace Research at the University of Notre Dame. Our comparative analysis of the fully

overlapping beams demonstrated strong agreement between the OPD fields reconstructed from each wavelength, with differential errors largely independent of flow speed. The root-mean-squared spatial error between the beams was relatively low, about 15%-20%, validating the method's ability to reconstruct the same optical field from independent beams. Simultaneous wavefronts over two apertures with two beam separations were measured over the range of subsonic speeds. Time-lag cross-correlation analysis between the spatially separated beams yielded convective speed estimates which indicated consistent scaling with freestream velocity, demonstrating the ability to capture dynamic measurements. While measurable error sources still exist when comparing reconstructed wavefronts and known flow properties, the results demonstrate that dual-wavelength digital holography holds strong potential for high spatial-resolution measurement of aero-optically aberrated wavefronts at different spatial regions of the flow.

Future work will include tracking down and eliminating various possible sources and issues contributing to the difference between the wavefronts for the fully overlapping case. Additional measurements of the wavefronts for different beam separations will also be conducted to investigate larger-than-expected values of the convective speeds.

This technique is scalable to additional wavelengths, only constrained by the ability to separate multiple beams in Fourier space and increased noise associated with each additional beam. Future work will focus on applying this approach to flows with stronger density gradients like shocks, where dual-wavelength fully overlapping beams are expected to significantly improve phase unwrapping and wavefront reconstruction.

Acknowledgments

This work was sponsored by the Joint Directed Energy Transition Office. The authors would also like to thank Zareb Noel for his help with the optical setup.

Disclosures

The U.S. Government is authorized to reproduce and distribute reprints for governmental purposes notwithstanding any copyright notation thereon.

Distribution Statement A. Approved for public release: distribution is unlimited.

REFERENCES

[1] Gordeyev, S., Jumper, E. J., and Whiteley, M., [*Aero-Optical Effects: Physics, Analysis and Mitigation*], Wiley (2023).

[2] Kalensky, M., Gordeyev, S., Kemnetz, M. R., and Spencer, M. F., "Aero-optical effects, part ii. sources of aberrations: tutorial," *J. Opt. Soc. Am. A* **41**, 2175–2187 (Nov 2024).

[3] Kalensky, M., Gordeyev, S., Kemnetz, M. R., and Spencer, M. F., "Aero-optical effects, part i. system-level considerations: tutorial," *J. Opt. Soc. Am. A* **41**, 2163–2174 (Nov 2024).

[4] Wilcox, C. C., Radosevich, C. J., Healy, K. P., Tuffli, A. L., Agena, B. D., Spencer, M. F., and III, D. J. W., "Digital holography wavefront sensing with a supersonic wind tunnel," in [*Holography: Advances and Modern Trends VI*], Fimia, A., Hrabovský, M., and Sheridan, J. T., eds., **11030**, 110300L, International Society for Optics and Photonics, SPIE (2019).

[5] Banet, M. T., Spencer, M. F., and Raynor, R. A., "Digital-holographic detection in the off-axis pupil plane recording geometry for deep-turbulence wavefront sensing," *Appl. Opt.* **57**, 465–475 (Jan 2018).

[6] Chu, E. D., Bukowski, T. J., and Gordeyev, S., "Improved wavefront reconstruction for shack–hartmann wavefront sensor in the presence of shock-related distortions," *Optics Laser Technology* **187**, 112764 (2025).

[7] Spencer, M. F., "Spatial heterodyne," in [*Encyclopedia of Modern Optics (Second Edition)*], Guenther, B. D. and Steel, D. G., eds., 369–400, Elsevier, Oxford, second edition ed. (2018).

[8] Herráez, M. A., Burton, D. R., Lalor, M. J., and Gdeisat, M. A., "Fast two-dimensional phase-unwrapping algorithm based on sorting by reliability following a noncontinuous path," *Appl. Opt.* **41**, 7437–7444 (Dec 2002).

[9] Guo, R., Lu, S., Wu, Y., Zhang, M., and Wang, F., "Robust and fast dual-wavelength phase unwrapping in quantitative phase imaging with region segmentation," *Optics Communications* **510**, 127965 (2022).

[10] Gass, J., Dakoff, A., and Kim, M. K., "Phase imaging without 2π ambiguity by multiwavelength digital holography," *Opt. Lett.* **28**, 1141–1143 (Jul 2003).

[11] Kühn, J., Colomb, T., Montfort, F., Charrière, F., Emery, Y., Cuche, E., Marquet, P., and Depeursinge, C., "Real-time dual-wavelength digital holographic microscopy with a single hologram acquisition," *Opt. Express* **15**, 7231–7242 (Jun 2007).

[12] Guo, R. and Wang, F., "Compact and stable real-time dual-wavelength digital holographic microscopy with a long-working distance objective," *Opt. Express* **25**, 24512–24520 (Oct 2017).

[13] Khoo, T. C., Sharikova, A., and Khmaladze, A., "Dual wavelength digital holographic imaging of layered structures," *Optics Communications* **458**, 124793 (2020).

[14] Huang, M., Qin, H., and Jiang, Z., "Real-time quantitative phase imaging by single-shot dual-wavelength off-axis digital holographic microscopy," *Appl. Opt.* **60**, 4418–4425 (May 2021).

[15] Gordeyev, S., Jumper, E., and Whiteley, M., [*Aero-Optical Effects: Physics, Analysis and Mitigation*], Wiley Series in Pure and Applied Optics, Wiley (2023).

[16] Gordeyev, S., Smith, A. E., Cress, J. A., and Jumper, E. J., "Experimental studies of aero-optical properties of subsonic turbulent boundary layers," *Journal of Fluid Mechanics* **740**, 214–253 (2014).

[17] Kemnetz, M. R., Burns, W. R., and Gordeyev, S., "Multiple aperture approach for the study of large-scale boundary-layer structures," in [*47th AIAA Plasmadynamics and Lasers Conference*], AIAA Paper 2016–3530 (2016).

[18] Kemnetz, M. R. and Gordeyev, S., "Multiple aperture approach to wavefront prediction for adaptive-optic applications," in [*55th AIAA Aerospace Sciences Meeting*], AIAA Paper 2017–1344 (2017).